ADVANCED MATERIALS
www.advmat.de

Ultra-Sensitive and Stable Multiplexed Biosensors Array in Fully Printed and Integrated Platforms for Reliable Perspiration Analysis

Suman Ma, Zhu'an Wan, Chen Wang, Zhilong Song, Yucheng Ding, Daquan Zhang, Chak Lam Jonathan Chan, Lei Shu, Liting Huang, Zhensen Yang, Fei Wang, Jiaming Bai, Zhiyong Fan, and Yuanjing Lin**

Electrochemical biosensors have emerged as one of the promising tools for tracking human body physiological dynamics via non-invasive perspiration analysis. However, it remains a key challenge to integrate multiplexed sensors in a highly controllable and reproducible manner to achieve long-term reliable biosensing, especially on flexible platforms. Herein, a fully inkjet printed and integrated multiplexed biosensing patch with remarkably high stability and sensitivity is reported for the first time. These desirable characteristics are enabled by the unique interpenetrating interface design and precise control over active materials mass loading, owing to the optimized ink formulations and droplet-assisted printing processes. The sensors deliver sensitivities of 313.28 µA mM^{-1} cm^{-2} for glucose and 0.87 µA mM^{-1} cm^{-2} for alcohol sensing with minimal drift over 30 h, which are among the best in the literature. The integrated patch can be used for reliable and wireless diet monitoring or medical intervention via epidermal analysis and would inspire the advances of wearable devices for intelligent healthcare applications.

1. Introduction

Wearable biosensors are of increasing importance for active real-time monitoring of human health, especially when combined with personalized therapies and disease prevention.[1–6] Commercially available technologies for human physiological biomarkers monitoring normally rely on invasive blood testing or minimal-invasive interstitial fluids analysis. These would introduce infection risks to the patient due to impaired wound healing and pain from acupuncture treatment, and thus fail to fulfill the demand for continuous and long-term health monitoring.[7–9] Therefore, it has attracted intensive research interest in developing non-invasive biomarkers analysis through body fluids such as sweat, tears,

---

S. Ma, Z. Wan, C. Wang, Z. Song, Y. Ding, D. Zhang, C. L. J. Chan, L. Shu, Z. Fan
Department of Electronic and Computer Engineering
The Hong Kong University of Science and Technology
Clear Water Bay, Kowloon, Hong Kong SAR 000000, China
E-mail: eezfan@ust.hk

S. Ma
Department of Materials Science and Engineering
Shenzhen Key Laboratory of Full Spectral Solar Electricity Generation (FSSEG)
Southern University of Science and Technology
Shenzhen 518055, China

Z. Song
Key Laboratory of Zhenjiang
Institute for Energy Research
Jiangsu University
Zhenjiang, Jiangsu 212013, China

L. Huang, Z. Yang, F. Wang, Y. Lin
School of Microelectronics
Southern University of Science and Technology
Shenzhen 518055, China
E-mail: linyj2020@sustech.edu.cn

J. Bai
Department of Mechanical and Energy Engineering
Southern University of Science and Technology
Shenzhen 518055, China

The ORCID identification number(s) for the author(s) of this article can be found under https://doi.org/10.1002/adma.202311106

DOI: 10.1002/adma.202311106

and saliva. Particularly, human eccrine sweat contains rich biomarkers including electrolytes (Na^+, Ca^{2+}, K^+, Cl^-), metabolites (glucose, urea, lactate), nutrition, and hormones.[10–23] However, practical and reliable long-term biosensing applications are largely limited by the challenges to realize highly stable biosensors, which mainly rely on the sensor's interface engineering. Generally, biosensors with rational interface optimization could deliver enhanced mechanical robustness and ion/electron transfer, while the signal drift can be largely mitigated. Apart from this, a multiplexed sensing array is also a practical strategy to improve reliability. On the one hand, a single biomarker analysis might result in misdiagnosis. For example, for diabetes patients, glucose is an important biomarker, whereas alcohol intake can alter glucose homeostasis, leading to false readings of blood glucose levels.[24,25] On the other hand, highly selective biosensing can be achieved with enzymatic sensors, while the enzyme activity can be largely affected by pH and temperature variation, thus resulting in sensing inaccuracy.[26,27] Therefore, there is an imperative demand for the development of ultra-stable sweat biosensing devices that are capable of simultaneously detecting multiple analytes to realize accurate and reliable health monitoring. Such devices could have possible applications in diet regulation, fitness monitoring, and medical intervention situations such as alcoholism, fluid imbalance, and hypoglycemia.

Conventional fabrication techniques, such as electrodeposition and drop coating, have been widely used for electrochemical device fabrication, while they show limited device uniformity and reproducibility.[28–32] As an alternative approach, inkjet printing offers the desired compatibility, versatility, and controllability for the construction of multiple sensors and integrated systems on flexible and wearable platforms.[33–44] However, the strict rheological criteria (viscosity and surface tension) on the ink formulations make it challenging to achieve fully inkjet-printed electrochemical sensors with desirable performance. To tackle this challenge, well-optimized ink formulations are required to ensure a smooth printing process and precisely optimize the active layer thickness. Additionally, the droplet-assisted process can produce seamless and uniform interpenetrating interfaces between layers, improving the mechanical adhesion and electron transfer between sensor layers. The robust interfaces can also eliminate aqueous layer formation. The high controllability ensures adequate active materials mass loading without introducing large impedance, thereby facilitating charge transfer. Based on this, the inkjet printing technology provides a promising strategy to enhance sensitivity, suppress signal drift, and enable long-term stability and lifespan of sensors.

Herein, we report a fully printed and multiplexed sensing (FPMS) system that delivers ultra-high sensitivity and long-term stability for continuous and wireless monitoring of multiple sweat biomarkers via non-invasive sweat analysis. The integrated system mainly consists of an electrochemical sensors array for selective biomarker tracking, and a customized flexible circuit for signal conditioning, processing, and wireless data transmission to mobiles via Bluetooth. The multiplexed sensors array integrates glucose and alcohol enzymatic sensors for simultaneous detection of multiple analytes, accompanied by pH and temperature sensors for in situ bio-signals calibration to ensure sensing accuracy. Besides, to construct the flexible sensors array through a maskless inkjet printing approach, 11 kinds of printable functional inks were systematically designed and optimized. Attributed to the desired controllability of active materials mass loading via inkjet printing, the lowest detection limit, sensitivities, and linear response ranges of the sensors can be well-tuned to fulfill sweat biomarkers monitoring applications. The as-printed sensors deliver remarkable sensitivities of 313.28 $\mu A\ mM^{-1}\ cm^{-2}$ to glucose and 0.87 $\mu A\ mM^{-1}\ cm^{-2}$ to alcohol, respectively, representing a state-of-art performance among the inkjet printing enzyme-based technologies. Most importantly, the as-printed active layers possess uniform porous morphologies and unique interpenetrating interfaces, which facilitate molecular/ion interactions and charge transfer to support long-term artificial sweat monitoring of up to 30 h. The fully printed sensors reveal minimal drift of around 0.08, 0.06, and 0.09 $mV\ h^{-1}$ for glucose, alcohol, and pH sensing, respectively. With the highly enhanced performance of individual sensor units, in situ bio-signals self-calibration within an array, and rational electronic integration, the accuracy and reliability of the extracted bio-signals from the FPMS system were validated for real-time sweat glucose and alcohol monitoring under different scenarios. The developed methodology to construct our unique FPMS system here can shed light on the design and fabrication of advanced wearable platforms for comprehensive and reliable human body health status analysis.

2. Results

2.1. Design and Fabrication of FPMS System

The structural details of the sensors and the framework of the FPMS system are illustrated in **Figure 1**. As shown in Figure 1a, the sensors for simultaneous and selective detection of glucose, alcohol, pH, and temperature are fabricated through a fully inkjet printing technique in a maskless manner on a flexible polyethylene terephthalate (PET) substrate. The sensor array is then integrated into a flexible circuit for intelligent epidermal biosensing (Figure 1b,c). The device architecture for the multiplexed sensors array is illustrated in Figure 1d with the specific fabrication detailed in the Experimental Section and Figure S1, Supporting Information. Briefly, commercial silver (Ag) ink is applied for the versatile patterning of current collectors for all the sensors, followed by the drop-on-demand printing of different functional inks on the electrodes to construct enzymatic amperometric glucose/alcohol sensors, non-enzymatic potentiometric pH sensors, and resistive temperature sensors. The sensors for glucose, alcohol, and pH analysis are based on a two-electrode configuration consisting of selective working electrodes and reference electrodes. The working electrodes for glucose and alcohol selective sensing consist of a conductive layer, transducer layer, and enzymatic layer. Note that the printing of gold (Au) ink on the Ag electrode pattern is essential to ensure the sensor stability due to the insufficient antioxidant capacity, strong corrosion tendency, and difficult surface chemical modification of Ag.[45–48] Subsequently, Prussian blue (PB) is used as the electron mediator to diminish the overall reduction potential to around 0 V.[49,50] The glucose oxidase (GO_X) or alcohol oxidase (AO_X) is then printed, followed by the selectively permeable Nafion layers to ensure the effective immobilization and stability of the enzymes. As for the pH sensing electrode, polyaniline (PANI) nanowires are adopted as the

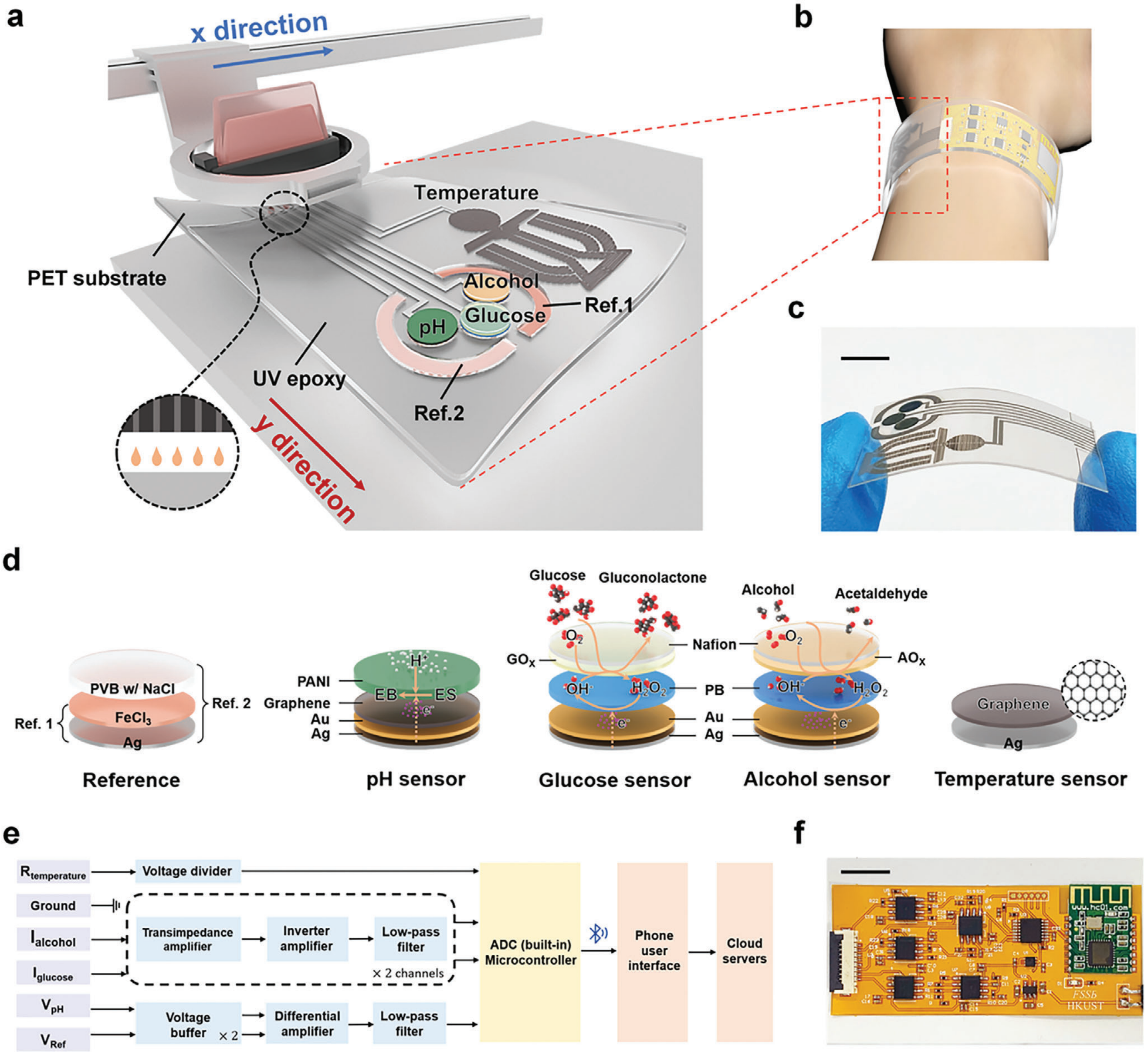

Figure 1. The fully printed integrated system for multiplexed epidermal sweat analysis. a,b) Schematic diagrams and c) photo of the fully printed sensor array for simultaneous multiplexed biosensing monitoring, including pH, glucose, alcohol, temperature, and reference sensing electrodes integrated on a PET substrate. Scale bar, 5 mm. d) Configurations of the sensor electrodes. e) System-level block diagram and f) photograph of flexible circuit patch containing signal conditioning, processing, and wireless transmission. Scale bar, 10 mm.

proton sensing membrane.[51,52] In an acidic solution, PANI absorbs H^+ ions, causing its bulk nitrogen atomic sites to become protonated. This results in a conductive emeraldine salt (ES), which induces a potential change. When the PANI is exposed to an alkaline solution, it loses H^+ and converts to an emeraldine base (EB). To increase the sensitivity, graphene quantum dots are used to modify the printed Au layer and serve as a cocatalyst.[53,54] In terms of reference electrodes, the one (ref. [1]) used for both glucose and alcohol sensors is silver/silver chloride (Ag/AgCl), which is formed by printing ferric chloride ($FeCl_3$) ink on the Ag and triggered the reaction to form AgCl. The second reference electrode in the pH sensor (ref. [2]) is Ag/AgCl/polyvinyl butyral (PVB), which suppresses the potential effect caused by the change of Cl^- concentration, and acts as a bridge between the electrolyte and sweat in the membrane.[55] As for temperature sensing, the graphene quantum dot ink is directly printed on an Ag pattern. UV epoxy is applied as the packing layer to complete the sensor array fabrication.[56] It is worth mentioning that the optimization of the functional inks and precise control of mass loading are critical to achieving biosensors with excellent performance. The signals obtained from the sensor array are then fed into the following flexible circuit patch for further processing (Figure 1e). The flexible circuit patch (Figure 1f) encompasses power regulation and signal processing units, together with a Bluetooth module, which are powered by a battery (Figure S2, Supporting Information). The system can extract low current signals (e.g.,<10^{-6} A) with minimal noise interference. The Bluetooth module enables the transmission of data to smartphones, which can be stored in the cloud afterward. A user interface is also developed to display the corresponding results of sweat analytes.

2.2. Synthesis and Optimization of the Printable Materials and the As-Printed Layers

A systematic study on the optimization and characterization of nanoengineered inks is conducted. As shown in **Figure 2a**, a variety of inks, including Ag, Au, PB, PANI, graphene, GO_X, AO_X, PVB, Nafion, and UV epoxy inks, are optimized to meet the surface tension and viscosity requirements for inkjet printing. Except for the commercial Ag ink, all the other ten kinds of functional inks are custom-designed. The composition and fluid physical properties of the inks are detailed in Table S1, Supporting Information. To prevent nozzle clogging, ultrasonic treatment and filtration are performed to prepare homogenous inks based on micro/nanoparticles in uniform sizes. Besides, sodium dodecyl sulfate (SDS) is added in the solvent to further ensure the effective dispersion such as for the PANI nanowires ink.

Attributed to the optimized ink formulation and droplet-assisted inkjet printing processes, uniform active layer morphologies and unique interpenetrating interfaces are observed (Figure 2 and Figures S6–S8, Supporting Information). To form a continuous and uniform conductive layer that serves as the foundation for the flexible sensor array, the printing parameters for Ag ink are optimized to ensure a smooth droplet ejection with proper drop distance (Figure S3 and Movies S1 and S2, Supporting Information), and maintain stable resistance under cycles of bending (Figure S5, Supporting Information). As shown in the scanning electron microscope (SEM) image, the printed Ag layer exhibits particle sizes between 50 and 100 nm (Figure 2b and Figure S6a,c, Supporting Information), and thus leaves the voids for Au nanoparticles with smaller particle sizes to penetrate into the upper layer of Ag (Figure 2c,d and Figure S6d,e, Supporting Information). Such interpenetration is also observed for graphene quantum dots printed on the Ag/Au and Ag (Figure S6g,h, Supporting Information), Ag/Au/PB layers (Figure 2f), and Ag/AgCl/PVB reference electrodes (Figure S8b,e,f, Supporting Information). Thus, the side reaction of Ag can be largely eliminated without direct exposure to the analytes in fluid samples, and maintain the conductivity to facilitate charge transfer. Additionally, the as-printed layers show uniform morphology and thickness (Figures S6f,i and S8d,e, Supporting Information).

Note that the ink formulations require careful design to avoid side reactions between active layers during the printing process, especially for the as-printed PB and PANI which play critical roles in ensuring sensor functionality. The desired product of PB printed with the potassium chloride (KCl) stabilized ink is validated with X-ray diffraction (XRD) and X-ray photoelectron spectroscopy (XPS) characterizations (Figure 2g and Figure S7, Supporting Information). PANI can exist in various forms, making it difficult to determine the exact form of fabricated PANI using XRD analysis of the initially synthesized nanowires. Before XRD analysis, the synthesized PANI can convert into ES and EB states, respectively. This conversion process is essential in determining whether the product is PANI (as shown in Figure 2j) and demonstrates its capability to realize sensitive proton sensing through a redox reaction. Exceptionally, the formation of Ag/AgCl is triggered by the oxidation reaction with printed $FeCl_3$ (Figure S8a,c, Supporting Information). Such interpenetrating interfaces with uniform morphology and thickness would significantly contribute to the highly enhanced sensitivity and stability of the fully printed biosensors.

2.3. Systematic Optimization and Characterization of the Fully Inkjet-Printed Biosensors Array

To achieve ultra-high sensitivities and stabilities with minimized drift, the mass loading of printable materials is carefully optimized and the sensing performances of the as-fabricated fully printed biosensors array are systematically characterized. **Figure 3a** shows the sensor responses under different concentrations of glucose in a phosphate-buffered saline (PBS) (pH 7) at room temperature. With optimization on PB and enzyme mass loading (Figures S12 and S13c, Supporting Information), the extracted sensitivity of the glucose sensor reaches 313.28 µA mM^{-1} cm^{-2} in the linear response range of 20–200 µM, which well fulfills the requirement of sweat glucose monitoring.[57,58] At the same time, the glucose sensors show good selectivity with negligible response to interfering substances such as urea, KCl, and sodium chloride (NaCl) (Figure 3b and Figure S14a, Supporting Information). Compared with reported works on inkjet printed sensors, the as-prepared glucose sensors deliver over 500% enhancement in sensitivity among the highly selective enzyme-based sensors (Table S2, Supporting Information). Since glucose oxidase activity can be affected by pH and temperature, the effects of different temperatures at pH 7 and different pH at room temperature on the performance of the sensor are systematic studies to facilitate in-array bio-signals calibration. It can be seen that the sensitivity and response current increase significantly with rising temperature (Figure S11a, Supporting Information), indicating an activation of GO_X catalytic property.[59] Similarly, when the pH rises from 4 to 7 (Figure S11b, Supporting Information), the sensitivity of the sensor also increases. The correlation between glucose sensing response and pH/temperature is displayed in Figure 3c.

The alcohol sensors have a similar device architecture to glucose sensors, except for the enzymes. Thus, it mainly requires optimization on the mass loading of the transducer PB layer and AO_X (Figure S13d–f, Supporting Information) to fit the required sensing range, while the fabrication of the Au/Ag current conductor and Nafion passivation layer remains the same. The highly selective alcohol sensors deliver an optimal sensitivity of 0.87 µA mM^{-1} cm^{-2} in the range of 5–30 mM (Figure 3d,e and Figure S14b, Supporting Information). The impact of pH and temperature variation on different oxidase activities is fitted in Figure 3f, which is consistent with the previous reports.[60,61] In contrast to glucose sensors, it is found that the sensitivity and corresponding current value of the sensor decreases as the ambient temperature increases from room temperature to 40 °C (Figure S11c, Supporting Information). While for varying pH, the sensor responses to

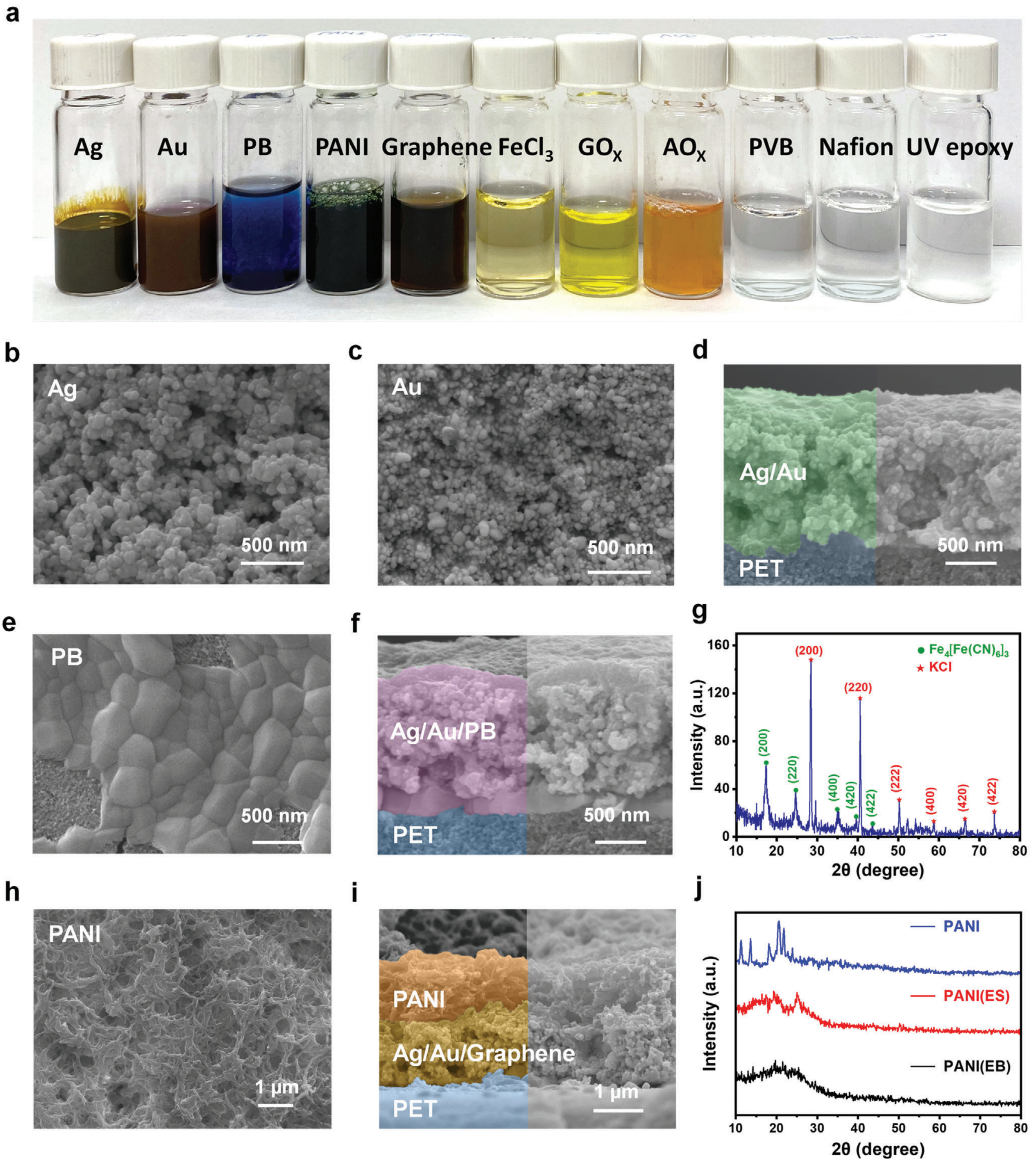

Figure 2. Characterization of inkjet printing inks for sensor fabrication. a) Photograph of the nanoengineered inks used to prepare the multiple sensors. SEM images of the inkjet-printed b) Ag, c) Au, d) as-form Ag/Au interpenetrating interface (cross-sectional view), e) PB, f) as-form Ag/Au/PB interpenetrating layer (cross-sectional view) on a nanotextured PET substrate. g) XRD spectra of PB ink. SEM images of inkjet-printed h) PANI and i) Ag/Au/Graphene/PANI interpenetrating layer (cross-section) on PET substrate. j) XRD spectra of PANI ink that can be converted to different redox states of PANI (ES) and PANI (EB).

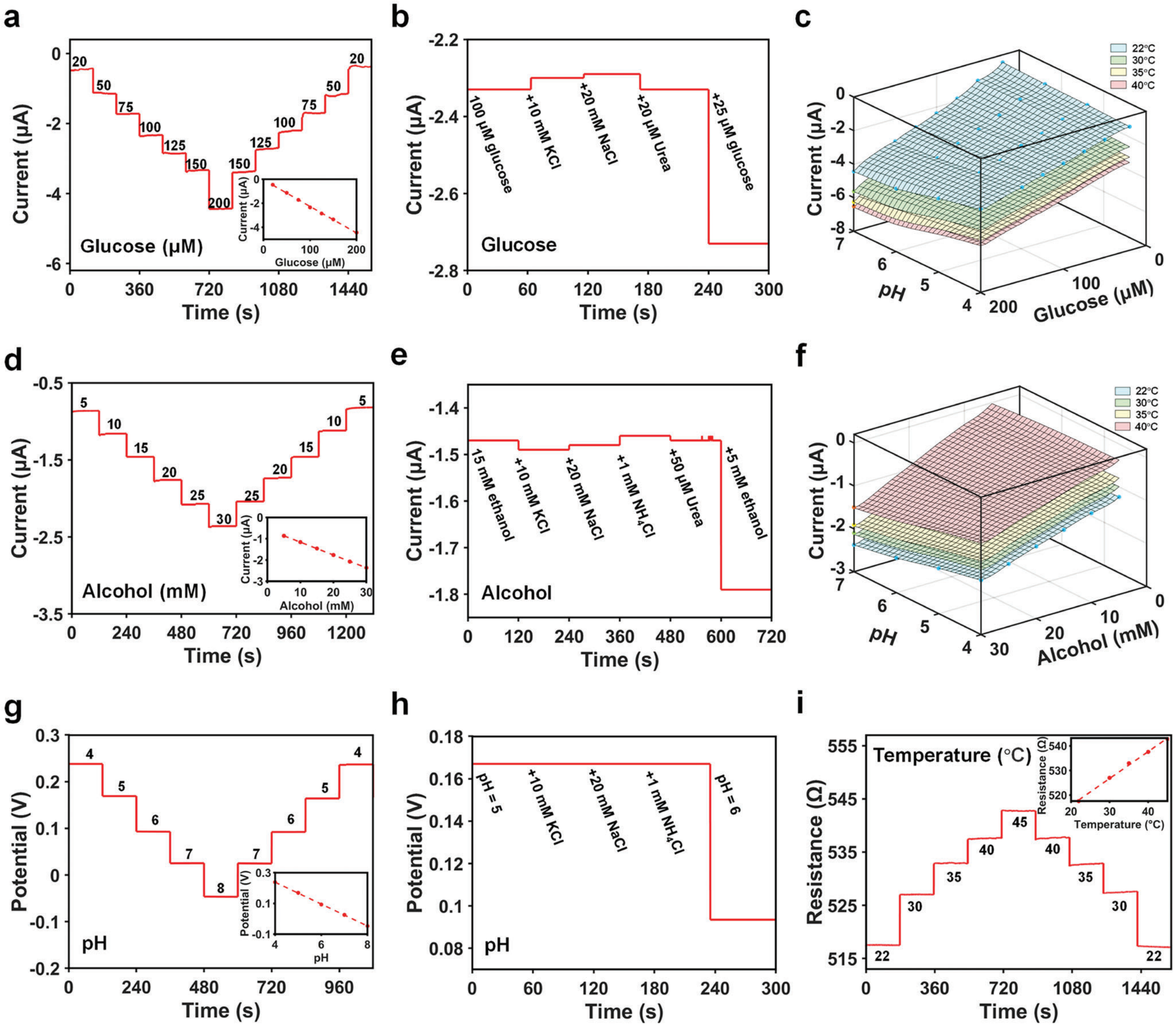

Figure 3. Experimental characterizations of fully printed multiplexed sensors. a) Amperometric response (R^2 = 0.998) and b) selectivity of glucose sensor (pH = 7, room temperature). c) The correlation of glucose sensing response with pH and temperature variation. d) Amperometric response (R^2 = 0.995) and e) selectivity of alcohol sensor (pH = 7, room temperature). f) The correlation of alcohol sensing response with pH and temperature variation. g) Potentiometric response (R^2 = 0.998) and h) selectivity of pH sensor. i) Resistive response of temperature sensor (R^2 = 0.996).

alcohol increase with rising pH (Figure S11d, Supporting Information).

The pH and temperature sensors in the array for bio-signals calibration are also characterized. The printed pH sensors modified with PANI nanowires and graphene quantum dots exhibit a desirable sensitivity of 71.125 mV per decade in normal human sweat pH range of 4 to 8 (Figure 3g), which is among the highest of printed pH sensors (Table S3, Supporting Information). The specific optimized parameters for the as-fabricated pH sensor are shown in Figure S16a–c, Supporting Information, and the selectivity toward H^+ is verified in the presence of K^+, Na^+, and NH4$^+$ (Figure 3h). It is also observed that the temperature variation has a negligible impact on the pH sensing performance (Figure S16d, Supporting Information). To achieve printed resistive temperature sensors without being interference by the sweat analytes, the Ag/Graphene electrodes are passivated with UV epoxy (Figure S17a, Supporting Information).

Attributed to electron-phonon scattering,[62–64] the graphene-based temperature sensors deliver a linear resistivity increase with temperature rising from 22 to 45 °C (Figure 3i). It reaches a sensitivity of 1.098 Ω $°C^{-1}$ with excellent stability during heating and cooling cycles, which is also validated by the consistent resistance extracted by voltammetric scan at different temperatures (Figure S17b,c, Supporting Information). Tables S2–S6, Supporting Information, show the comparison of fully printed sensors with other works and summarize the multiplexed sensing platform.

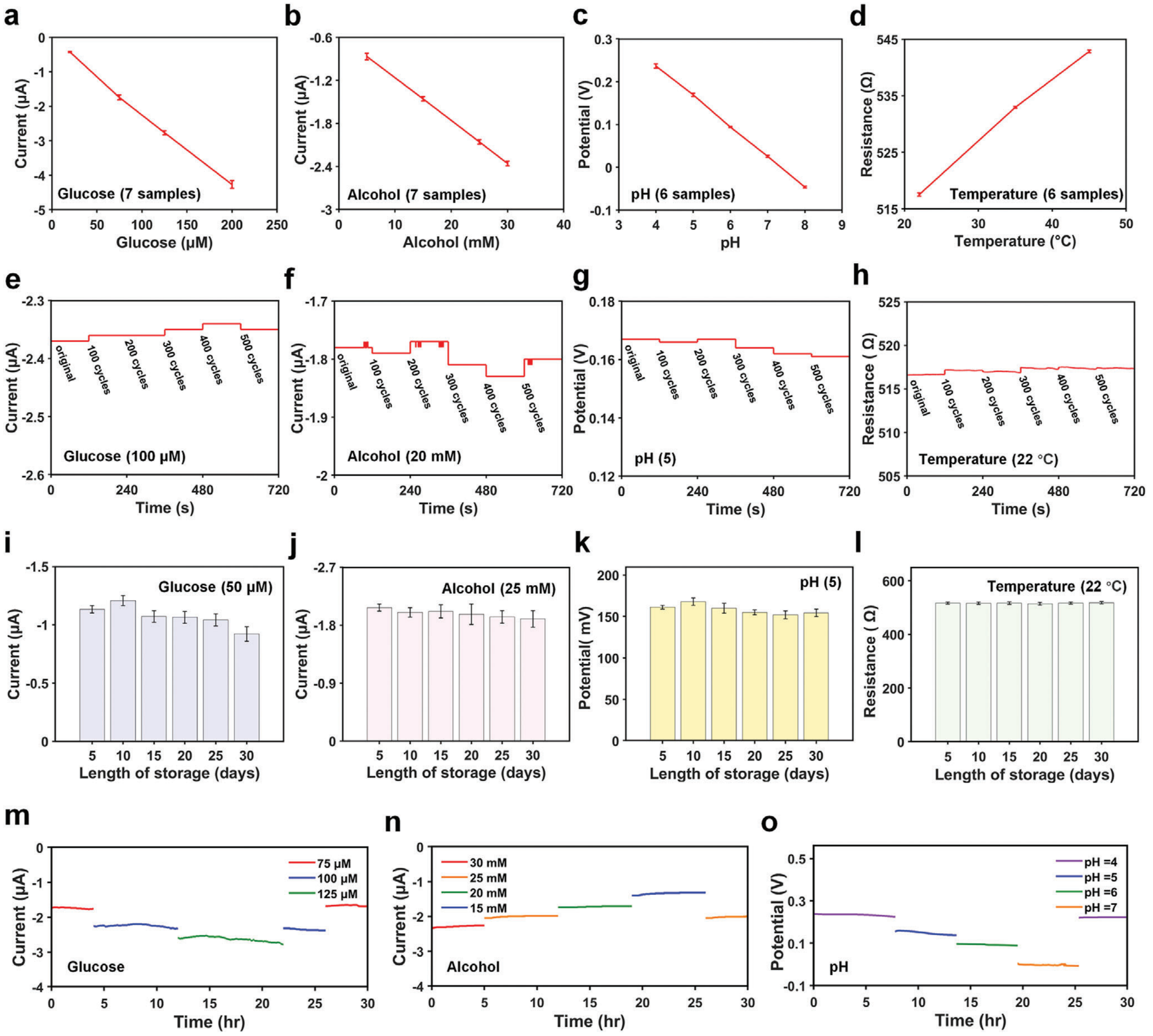

Figure 4. Reproducibility, bendability, and stability evaluation of the fully printed flexible sensor array. Reproducibility of a) glucose sensors (7 samples), b) alcohol sensors (7 samples), c) pH sensors (6 samples), and d) temperature sensors (6 samples). Bendability test of e) glucose sensor, f) alcohol sensor, g) pH sensor, and h) temperature sensor after 0, 100, 200, 300, 400, and 500 cycles of bending 135°. Long-term stability of i) glucose sensor, j) alcohol sensor, k) pH sensor, and l) temperature sensor (60 min/day). Long-term continuous measurement of m) glucose sensor, n) alcohol sensor, and o) pH sensor.

The optimized glucose, alcohol, pH, and temperature sensors are then integrated into a sensor array. The reproducibility, bendability, and stability of the sensor array are characterized and displayed in **Figure 4**. The remarkable reproducibility (Figure 4a–d) of the sensor array emphasizes the high controllability of inkjet printing in sensor fabrication. The mechanical stability of the inkjet-printed sensors was tested using repeated bending and adhesion tests. After 500 times of 135° bending, the interferences of mechanical stress on the analytical performance of the sensor were less than 3% (Figure 4e–h), demonstrating its capability for wearable applications. It is found that the trend of the temperature sensor resistance change (Figure 4h) is similar to that of the Ag electrode resistance change (Figure S5, Supporting Information), indicating that the effect of bending on the sensors might be from the Ag layer. Furthermore, the electrodes show negligible variations in the surface morphologies (Figure S18, Supporting Information). The working electrodes of glucose and alcohol sensors, as well as the temperature sensors, remain similar surface morphologies after bending. It can be possibly attributed to the desirable mechanical stability of the thin Nafion/UV layers on top of the sensors. Small cracks appeared on the surface of the pH working electrode and the Ag/AgCl (ref. [1]) reference electrode after 500 times bending. Additionally, wrinkles appeared on the relatively thick PVB layer on the surface of the Ag/AgCl/PVB

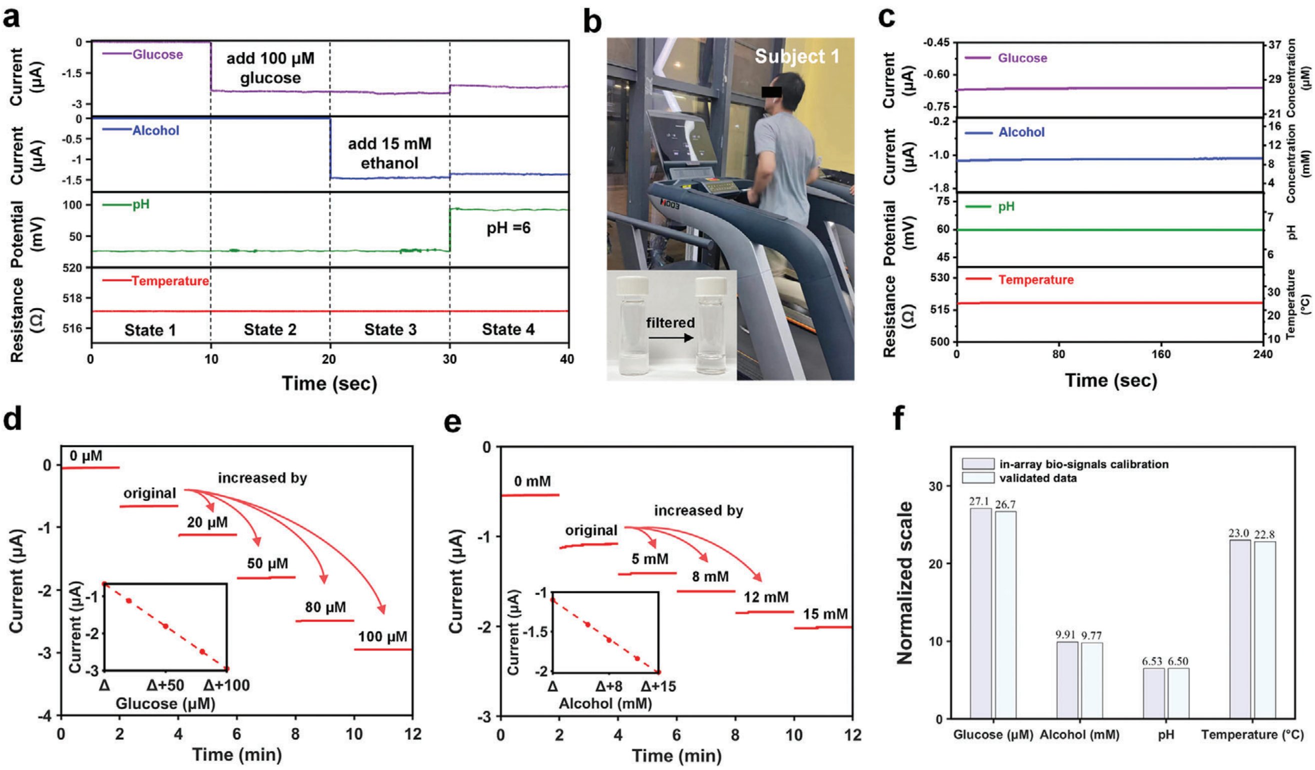

Figure 5. Reliability evaluation of the integrated FPMS system with in-array bio-signals calibration. a) Sensors response to artificial sweat testing with varying analyte concentrations at room temperature. b) Sweat sample collected when Subject 1 (male) is running after drinking a bottle of beer. c) Extracted signals (left *y*-axis) and decoded analytes concentrations (right *y*-axis). d) Glucose (R^2 = 0.995) and e) alcohol (R^2 = 0.992) concentrations validation by using interpolation method. f) Comparison of the decoded analytes concentrations with in-array bio-signal calibration and validated data.

(ref. [2]). Besides, the adhesion between the printed sensing electrodes and the PET substrates was measured using the pull-off test method, which further indicates the desirable mechanical stability for wearable applications (Figure S19, Supporting Information).

In addition, the long-term stability of the sensor array, including storage lifetime and continuous sensing performance, is evaluated. In Figure 4i–l, the four kinds of sensors are tested in solutions for 30 days (60 min a day). The minor response current drop of glucose and alcohol sensors could be mainly attributed to the decreasing oxidase activity. The minimized variation of pH sensitivity can be due to the unattached PANI nanowires shedding into the solution, while the resistance of the temperature sensor remains extremely stable. The sensors are used to continuously monitor the artificial sweat with varying concentrations for up to 30 h, and the corresponding drifts of glucose, alcohol, and pH sensor are estimated around 0.08 μA h^{-1}, 0.06 μA h^{-1}, and 0.09 mV h^{-1}, respectively (Figure 4m–o). When tested in artificial sweat samples with relatively constant concentrations, the sensors show promising long-term stability of up to 50 h (Figures S20–S22, Supporting Information) without delamination of active layers. Such continuous sensing stability of a fully printed multiplexed biosensor array has been rarely reported and would no doubt inspire the advance of biosensing devices for practical applications.

2.4. Reliability Validation of the FPMS System for On-Body Perspiration Analysis

The integrated FPMS system is evaluated for its capability to eliminate the interference from sensors cross-talk the accuracy of signals processing in artificial sweat with multiple biomarkers. PBS (pH 7) containing 10 mM NaCl, 1 mM ammonium chloride (NH_4Cl), 10 mM KCl, and 10 μM urea was adopted as the initial artificial sweat. The integrated sensor is soaked in initial artificial sweat at room temperature (State 1), whereupon adding glucose to 100 μM (State 2), alcohol to 15 mM (State 3), and acid to a pH of 6 (State 4). As shown in **Figure 5**a, the corresponding sensors show rapid responses with minor cross-talk with interference from pH variation, while the resistive response of the temperature sensor remains constant. The test values obtained from the sensor array are consistent with those from individual sensors (Figure 3).

The FPMS is further characterized by real sweat samples collected from Subject 1(male), who drink a bottle of beer during a meal and run after 60-min rest (Figure 5b). Figure 5c shows the recorded amperometric, potentiometric, and resistive responses, and the sweat bio-markers concentrations are decoded to be corresponding 27.1 μM glucose, 9.91 mM alcohol, pH of 6.53 with temperature readout at 23 °C. These decoded values by referring to calibration references (as discussed in Figure 3c,f) are then

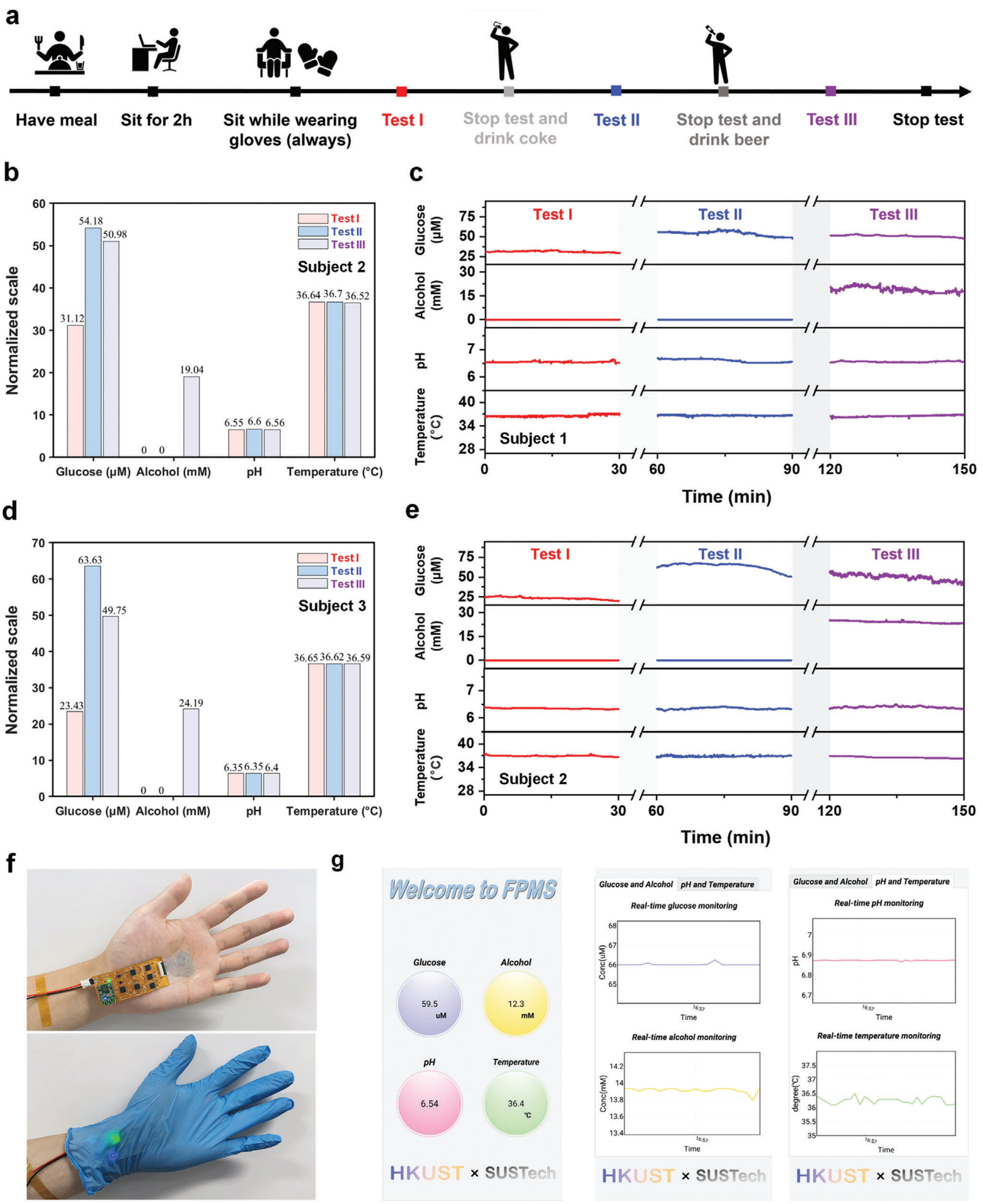

Figure 6. On-body and real-time epidermal sweat analysis with FPMS system. a) Schematics of the protocols to investigate the effect of glucose and alcohol intake. b) Average values of decoded glucose, alcohol, pH, and temperature level during Test I–III of male Subject 2. c) Real-time on-body analysis of perspiration analytes of Subject 2. d) Average values of glucose, alcohol, pH, and temperature sensors during Test I–III of female Subject 3. e) Real-time on-body analysis of perspiration of Subject 3. f) Photographs of a subject wearing FPMS system. g) Corresponding user interfaces.

validated. By adding artificial sweat to the real sweat samples with a series of concentration variations, the glucose and alcohol concentrations in the original sweat sample can be calculated via the interpolation method (Figure 5d,e). While the pH and temperature values can be validated with commercial meters. The in-array bio-signal calibration delivers a high accuracy of over 98% compared with validated data (Figure 5f), indicating the reliability of the FPMS system for biosensing applications.

The FPMS system with excellent sensitivity, stability, reproducibility, and bio-analyzing reliability is then applied for wearable in situ sweat monitoring. The real-time monitoring of sweat glucose, alcohol, pH, and epidermal temperature is performed on two subjects (male Subject 2 and female Subject 3) with schedules as shown in **Figure 6**a. The subjects are asked to sit casually for 120 min after taking the same meal, so as to allow basal metabolism. During this time, gloves are worn on the left hand to ensure the continuous production of perspiration without fast evaporation. When sufficient sweat is generated, the FPMS patch is stuck to the palm area in the glove and initiates the 30-min sweat monitoring with running (Test I). After completing Test I, a bottle of Coke containing sugar is supplied to each subject, and a 30-min rest is scheduled for digestion before another 30-min monitoring (Test II). Similarly, Test III is performed after drinking beer. Figure 6b,d summarizes the average level of targeted biomarkers. The multiplexed sensors array provided responses in a sensitive and highly selective manner. It indicates that sweat glucose and alcohol would be affected by intakes in a quite significant manner, as can be seen from the increased glucose level after Coke drinking (Test II), and the soaring sweat alcohol concentrations with beer (Test III). It is also observed that sweat glucose would decrease gradually (Figure 6c,e), while alcohol intake could possibly trigger glucose generation, as shown in the recorded data from Subject 3 (Figure 6e).[65] During the tests, the body temperature of both two subjects remained relatively stable within the range of 36.5–36.7 °C, and the pH variations were within 0.05. The as-decoded physiological monitoring results are in a reasonable tendency and consistent with the medical study.[64–69] The real-time monitoring data can be wirelessly displayed on mobiles (Figure 6f,g and Movie S3, Supporting Information) and further stored in cloud servers. Such successful demonstration of wearable and continuous sweat monitoring using the as-fabricated FPMS can be attributed to the excellent sensitivity and stability of the multiplexed sensors array, as well as the in-array bio-signals calibration capability of the integrated system.

3. Conclusion

In this study, we demonstrated a fully printed multiplexed sensing system on a flexible and integrated platform with excellent reliability and reproducibility for non-invasive analysis of perspiration biomarkers. The FPMS system allows continuous and simultaneous monitoring of sweat analytes based on multiplexed biosensing strategies including amperometric glucose and alcohol tracking, potentiometric pH sensing, and resistive temperature monitoring. With a systematic and in-depth study of the printable ink formulations and fabrication process, unique and uniform interdiffusion interfaces were created. Thus, attractive sensing performances including ultra-high enzymatic sensor sensitivity, remarkable long-term sensing stability with minimized signal drift, and desirable lifespan were achieved. Moreover, with in-array bio-signals calibration, the sensing accuracy of sweat analytes, such as glucose and alcohol concentrations in sweat, was significantly enhanced by considering the influence of pH and temperature variations. As a proof-of-concept, the as-fabrication biosensing system was successfully demonstrated for real-time sweat sensing with different kinds of drink intake. It is worth mentioning that the perspiration analysis was performed at rest status without intensive exercise to trigger sweating, showing its promising applications for daily health monitoring, especially for the elderly and chronic disease management such as diabetes. Such a fully printed fabrication strategy to construct a wearable integrated biosensing system would no doubt inspire the scalable fabrication of multi-modal sensors for advanced and intelligent personalized healthcare, pre-diagnosis, and Internet of Medical Things.

4. Experimental Section

Materials: PET (noveleTM pack, Novele IJ-220) and Ag nanoparticle ink (Metalon JS-B25HV) were purchased from NovaCentrix. Acetone, 2-propanol (IPA), methanol, ethylene glycol (EG), sodium hydroxide (NaOH), potassium ferricyanide ($K_3[Fe(CN)]_6$), hexacyanoferrate trihydrate ($K_4[Fe(CN)]_6$), iron(III) chloride hexahydrate ($FeCl_3 \cdot 6H_2O$), glucose, ethanol, urea, hydrochloric acid (ACS reagent, 37%) (HCl), KCl, NaCl, NH_4Cl, gold(III) chloride trihydrate (≥99.9% trace metals basis) ($HAuCl_4 \cdot 3H_2O$), polyvinylpyrrolidone (mol wt 360 000) (PVP), sodium borohydride ($NaBH_4$), aniline, ammonium persulfate (APS), SDS, chitosan, nafion perfluorinated resin solution (5 wt% in mixture of lower aliphatic alcohols and water, contains 45% water), GO_X from aspergillus niger (Type VII, lyophilized powder, ≥100 000 units g^{-1} solid (without added oxygen)), PBS (pH 7), sodium phosphate dibasic (Na_2HPO_4), and citric acid anhydrous were purchased from Sigma-Aldrich. Potassium phosphate monobasic (KH_2PO_4), PVB (M.W.40 000–70 000, Butvar B-98), AO_X (lyophilized powder, 5–15 units mg^{-1} protein), and graphene quantum dots (1 mg mL^{-1} tablet diameter 3–6 nm) were purchased from Aladdin. Potassium hydroxide (KOH) was purchased from Thermo Fisher Scientific. Ammonia (solution 28% w/w, reagent grade, Pharmpur) was purchased from Scharlau. Optical adhesive NOA81 was purchased from Norland. PH-indicator strips (pH 4–7, 5.2–7.2, 5–10, MQuant), were purchased from Supelco. Acrodisc syringe filters (Nylon membrane, diam. 13 mm, pore size 0.45 µm) were purchased from Pall Corporation.

Synthesis and Characterization of the Printable Inks: Hermle Z206A centrifuge was used for the centrifugation process. Crest Ultrasonics (2600PD132-1 Model P2600) was used for ink redispersing. The synthesis of Au nanoparticles can be referred to in other reports.[70] Briefly, 50 mg $HAuCl_4 \cdot 3H_2O$ was dissolved in 7.5 mL deionized (DI) water by magnetic stirring, to which 375 mg PVP was rapidly added. The mixture was stirred for 30 min. After that, 5 mL of 25 mg $NaBH_4$ and 1 м NaOH were prepared, stirred for 10 min, and then kept in the refrigerator for 30 min at 4 °C. Once the $NaBH_4$ solution was ready, 150 µL of the resulting solution was mixed with $HAuCl_4$ solution and left agitated for 6 h, leading to a solution in purple. The synthesized nanoparticles were rinsed by centrifuging the solution at 6000 RPM for 30 min, followed by removing the aqueous liquid, adding the same volume of DI water, and gently agitating the centrifuge tube. This rinsing step was repeated twice to thoroughly remove the unreacted oxidants and acids from the liquid. The precipitate was then redispersed in 3.5 mL DI water and 1.5 mL EG via ultrasonication for 30 min. Finally, the 0.6 mL dispersion was filtered through a 0.45 µm syringe filter and mixed with 0.2 mL EG (60:20, v/v) to form the Au ink. The XRD pattern (Figure S7c, Supporting Information) and energy dispersive spectrometer (EDS) image (Figure S7e, Supporting Information) confirmed that the metal product prepared was pure Au without other by-products.

PB ink was synthesized by a simple chemical method with minor modifications.[71] 2 mL of 2 mM $K_4[Fe(CN)_6]$ was mixed with 1 mL of 0.1 M KCl and 10 mM HCl. Subsequently, 2 mL of 2 mM $FeCl_3$ was added dropwise to the previous solution and stirred vigorously overnight. Finally, 0.6 mL of the resulting blue solution was filtered through a 0.45 μM syringe filter, and 0.15 mL of EG was added to obtain PB ink. EDS results showed that the main elements of the samples were Fe, N, C, K, O, and Cl (Figure S7b, Supporting Information). XPS spectra confirmed the existence of Fe 2p, O 1s, N 1s, K 2p, C 1s, and Cl 2p (Figure S7c, Supporting Information). Meanwhile, in the high-resolution spectrum of Fe 2p (Figure S7d, Supporting Information), two prominent peaks were observed at 708.75 and 721.6 eV, which could be assigned to $Fe^{II}2p_{3/2}$ and $Fe^{II}2p_{1/2}$, and two peaks at 710.27 and 724.57 eV, which belonged to $Fe^{III}2p_{3/2}$ and $Fe_{III}2p_{1/2}$, respectively. The XPS results were consistent with those reported in the literature.[72] The peak generated at 713.15 eV was due to the charge transfer mechanism associated with Fe^{III}, and some peaks of $Fe^{III}2p_{3/2}$ and $Fe^{II}2p_{3/2}$ were satellite peaks.[73] Furthermore, the high-resolution spectrum of C 1s (Figure S7e, Supporting Information) indicated the presence of C=O (288.5 eV), C—N (286.8 eV), C≡N (285.7 eV), and in this test, C 1s peak was shifted to 284.9 eV for energy calibration. The results confirmed the presence of carboxyl groups. Similarly, Figure S7f, Supporting Information, demonstrates the existence of N in the cyano ligands. In conclusion, the C≡N and Fe^{II} generated hexacyanoferric(II) acid as the inner layer through coordination bonds and connected with Fe^{III} in the outer layer through ionic bonds to form $Fe_4[Fe(CN)_6]_3$ (PB).

The reagents and methods required for the preparation of PANI are with references to a previous paper.[74] First, two different solutions, 10 mL of 0.08 M aniline in 1 M HCl and 10 mL of 0.02 M APS in 1 M HCl, were prepared. After continuous stirring for 30 min, the two resulting solutions were mixed and vigorously shaken up and down about 30 times. After leaving still for 4 h, PANI nanowires were synthesized. The dark green solution was centrifuged at 6000 RPM for 30 min. After removing the supernatant, an equal amount of DI water was added to repeat the centrifugation step twice. After that, 10 mL of DI water was added to the obtained precipitate, and 0.08 g of SDS surfactant was added and sonicated for 30 min in order to disperse the nanowires uniformly. The as-prepared PANI inks fulfill the viscosity and surface tension requirements of the inkjet printer.

The graphene ink was prepared by filtering 0.6 mL of graphene quantum dots solution through a 0.45 μM syringe filter and then adding 0.2 mL of EG to adjust the viscosity and surface tension. The GO_X ink was a mixed solution of 50 mg GO_X and 5 mL PBS. The ink needs to be refrigerated in the refrigerator to ensure the activity of GO_X. The AO_X ink was prepared by diluting 1 mL AO_X solution with 2.5 mL PBS. This ink must be frozen in the refrigerator to ensure the activity of AO_X. Meanwhile, it needed to be thawed before printing in an efficient manner. The $FeCl_3$ ink was prepared by mixing the 0.8 mL 0.1 M $FeCl_3$ solution with 0.3 mL EG (80:30, v/v). The PVB ink was first prepared by dissolving 0.6 g PVB and 0.4 g of NaCl into 8 mL methanol, and after stirring for 30 min, the supernatant obtained by 0.08 mL filtration was mixed with 0.85 mL methanol. The Nafion ink was prepared by diluting the Nafion solution (5% wt) with DI water at a ratio of 16:96 v/v. The UV epoxy ink was obtained by mixing 2.5 g Optical adhesive NOA81 and 5 mL acetone, stirring vigorously for 60 min, and filtering through a 0.45 μM syringe filter.

The dynamic viscosity, surface tension, and density of the inks, together with the inverse of the Ohnesorge number (Z), are shown in Table S1, Supporting Information, and the practical range of ink printability was $\approx 2 < Z < 20$.[75] All inks should be sonicated before printing to prevent agglomeration and ensure uniform dispersion.

Fabrication of the Inkjet-Printed Multiplexing Biosensors: The fabrication process of the fully inkjet-printed multiple sensors is illustrated in Figure S1, Supporting Information. The PET films were cleaned with IPA and acetone, and the rough side was used for printing. Dimatix Materials Printer (DMP-2800, Fujifilm) and Dimatix Materials Cartridge 10 pL (DMC-11610, Fujifilm) were used to achieve a balance of printing precision and efficiency. The 10 pL ink cartridge has 16 nozzles with a diameter of 21 μM. For all the inks utilized in this work, the waveform that controls the extruded ink from each nozzle is shown in Figure S4, Supporting Information. The electrode patterns were designed in a computer painting program and then imported into the Dimatrix Material Printer software.

The pattern was then printed on a PET substrate at room temperature with Ag ink.[76] To optimize the morphology of the Ag electrode, the Ag ink was printed with drop distances of 15, 20, 25, 50, and 80 μM on the PET substrate. It was found that the size of the Ag droplets was about 40 μM. To ensure the uniformity of the electrode pattern, the drop distance was selected as 20 μM (Figure S3, Supporting Information). The temperature of the printer plate was then adjusted to 55 °C and annealed for 30 min to ensure solvent evaporation.

Afterward, the temperature of the plate was lowered to 45 °C, and 40 layers of Au ink were printed on the working electrodes of the glucose, alcohol, and pH sensor. The addition of Au, although in small amounts (1% w/w), to the glucose and alcohol electrodes can significantly improve the stability and sensitivity of the sensor (Figures S13c,f and S15, Supporting Information). Each layer of ink was annealed on the plate for about 20 min to ensure solvent evaporation before the next round of printing.

For glucose and alcohol sensors, PB ink was printed on the working electrode area as the transducer layer. To better determine the number of PB layers required for inkjet printing, cyclic voltammetry of Ag/Au/PB containing different layers of PB was conducted in 0.1 M KCl solution at a scan rate of 100 mV s^{-1} (Figure S12, Supporting Information). The results indicated that the electron transport rate was the highest when the number of PB layers was 30. Based on this, the sensor performance ought to be optimized around 30 layers. The sensitivity of the glucose sensor was indeed the highest at PB of 30 layers, but the linear range was 20–150 μM. Although the sensitivity of the sensor with 35 and 40 layers of PB decreased, the linear range was extended (Figure S13a, Supporting Information). Therefore, a 35-layer PB was selected as the optimized parameter for glucose sensors. Similarly, the number of PB layers of the alcohol sensor was optimized to be 40 (Figure S13d, Supporting Information). At room temperature, 14 layers of GO_X ink and 12 layers of AO_X ink were printed on the working area of the sensor, respectively. To ensure the stability of the sensor and prevent the oxidase from falling off in the electrode area, the addition of a Nafion layer was essential. The number of printing layers of Nafion ink was three layers.

For pH sensors, six layers of graphene ink were printed on the working area of the pH sensor. Subsequently, 30 layers of PANI ink were also printed on the working area of the pH sensor to complete the fabrication of the working electrode. For temperature sensors, eight layers of graphene ink were printed on electrode patterns.

For reference electrodes, its performance optimization also played a critical role in the sensor sensitivity. The key factors for Ag/AgCl electrodes were the number of $FeCl_3$ layers and the annealing temperature. According to the optimized parameters, the temperature of the plate was adjusted to 40 °C, and six layers of $FeCl_3$ ink were printed on the Ag patterns (Figure S9, Supporting Information). As for the Ag/AgCl/PVB electrode, it was necessary to ensure that different interference concentrations and different pH would not introduce significant variation (Figure S10c, Supporting Information). Three layers of PVB ink were continuously printed on the Ag/AgCl electrode and dried at room temperature.

UV epoxy was utilized to encapsulate the non-working area of the sensor array and the temperature sensor area to reduce unnecessary contact with sweat and interference. This method was achieved by printing multiple layers of UV epoxy ink followed by curing with UV light. The printed inks and sensors were stored in the refrigerator at 4 °C.

Characterizations of the Inkjet-Printed Multiplexing Biosensors: Various analytical techniques were utilized to characterize the sensors. The electrochemical measurements were performed using a CHI 1000c Electrochemical Workstation Analyzer (CH Instruments, Inc). The performances of the glucose and alcohol sensors were tested chronoamperometrically in PBS buffer solution with varying glucose/alcohol concentrations and pH values based on a two-electrode configuration. The pH sensor was tested with different McIlvaine buffers. All measurements were paused while refreshing solutions and continued after a waiting period of 120 s. For reference electrode optimization and testing, a three-electrode configuration was adopted. Graphite and platinum were used as the counter and working electrodes, respectively. The printed Ag/AgCl reference electrodes were compared with commercial reference electrodes in terms of the redox reaction of $[Fe(CN)_6]^{3-}/[Fe(CN)_6]^{4-}$ via cyclic voltammetry scanning at the scan rate of 100 mV s^{-1}. The optimized printed electrode that produces the closest redox potential to the commercial reference electrode can be prepared with six layers of Ag/AgCl ink printing and annealing at 40 °C. The testing solution contained 0.1 м KCl, 0.1 mм $K_3[Fe(CN)_6]$, and 1 mм $K_4[Fe(CN)_6]$ (Figure S9, Supporting Information). The long-term stability was verified with the open-circuit potential between the printed Ag/AgCl and a commercial reference in different NaCl concertation solutions (Figure S10a,b, Supporting Information).

The resistive responses of temperature sensors were recorded using a Keithley 2450. The bendability test of printed electrodes was measured with the MIT Folding Endurance Tester (Guangdong AISRY Instrument Technology Co. Ltd.). The surface tension of different inks was measured by a Contact Angle Meter (Biolin Scientific Theta Lite), and dynamic viscosity was characterized with NDJ-8S Digital Rotary Viscometer (Shanghai Lichen Technology). The morphology of sensors was characterized by SEM (JSM-7100F, JEOL). EDS mapping was achieved by a high-resolution transmission electron microscope (HR-TEM, JEM 2010F, JEOL). Element characterization was done by XRD (X'pert Pro (PANalytical)) with a take of angle at 90°. XPS was conducted to characterize chemical states analysis (Physical Electronics 5600 multitechnique system, Physical Electronics, Inc. (PHI)).

Wearable Circuit and Mobile Application Design: The FPMS system was powered by a 3.7 V rechargeable lithium-ion polymer battery and utilized a 12-bit ADC microcontroller based on STM32L011D4 for signal conditioning, processing, and wireless transmission via Bluetooth. The glucose and alcohol sensors shared a reference/counter electrode for current readout. The low-power OPA2145 was selected to build a transimpedance amplifier to amplify the signals and then convert it into positive voltage signals. To ensure that voltage and current readout do not interfere with each other, the pH sensor was coupled with a separate PVB reference electrode. The potentiometric response of the pH sensor passed through two voltage buffers and generated a differential voltage, followed by a low-pass filter to minimize noise. The temperature sensor resistance was measured by dividing the voltage with a 510 Ω resistor at 3.3 V. The schematic diagram, illustration of the flexible circuit patch electronic system, and photographs of the wearable FPMS are shown in Figures S2, S23, and S24, Supporting Information, respectively. The mobile application interface was composed of multiple modules, and users can read the calibrated real-time measurement results of glucose, alcohol, pH, and temperature and display the graphs. The data can be further uploaded to the cloud server.

On-Body Epidermal Sweat Analysis Using FPMS System: On-body human-participant trials were conducted in compliance with the human research protocol (2020SGW138) approved by the Institutional Review Board (IRB) of the Southern University of Science and Technology. Subjects between the ages of 20 and 30 were informed and consented to the risks and benefits of the trials. Prior to the on-body trials, subjects consumed the same diet and rested for 2 h, washed their hands with soap and water, and wiped them with gauze before attaching the integrated FPMS patch to the palm with polyimide adhesive tape. The trials were carried out in a ventilated laboratory environment at 23–25 °C and 35–45 % relative humidity. The signal extraction and process were started ≈30 min after the glove was worn to ensure sufficient sweat had accumulated for reliable measurements. Sensors were calibrated before and after body data collection to convert raw signals into accurate concentration estimates.

Off-Body Epidermal Sweat Analysis Using FPMS System and Data Validation: The alcohol and glucose concentrations of real sweat samples were validated with the interpolation method. Sweat samples were collected every 1 s around the same skin area in microtubes for off-body data validation. For glucose sensing results validation, the current value of the glucose sensor was first obtained in the solution without glucose. After thoroughly drying, an amount of 2 µL of sweat was applied to the sensors, and the current responses were recorded. The concentration of glucose in the sweat was then increased for a series of values by adding an additional glucose solution, and the corresponding responses were recorded. The slope k is obtained from the straight-line fitting of the relationship between the recorded sensor output currents and the concentrations. The current value of the solution without glucose is b. The glucose concentration in the original sweat can be calculated from $y = kx + b$, where y is the current, and x is the concentration. The alcohol concentration was validated in the same way. The pH values were validated with a pH meter and the temperature with a thermometer.

Statistical Analysis: All data are presented without further processing unless the fitting strategy for the XPS. The XPSpeak software was used for the peak fitting, and Newton's method was selected for the fitting. All data were plotted through Origin software, except for Figure S4, Supporting Information, which was screenshotted through inkjet printing software. The fitted parameters correlation coefficient was presented as the goodness of fit r-squared (R^2) in figure legends of Figures 3a,d,g and 5d,e. R^2 values were computed using Origin software. The sample sizes are displayed in Figure 4a–e. There was no removal or adjustment of the collected data.

Supporting Information

Supporting Information is available from the Wiley Online Library or from the author.

Acknowledgements

The authors thank Mr. Nick K C HO and Miss Christine P Y CHEUNG from the Material and Characterization Preparation Facility (MCPF) at HKUST for technical assistance with XPS and XRD characterizations, and the technical support from SUSTech CRF. This work was financially supported by Foshan HKUST projects (FSUST21-HKUST08D, FSUST21-HKUST09D) and Foshan Innovative and Entrepreneurial Research Team Program (2018IT100031), National Natural Science Foundation of China (Project No. 62 201 243), Fundamental and Applied Research Grant of Guangdong Province (2021A1515110627), Shenzhen Stable Support Plan Program for Higher Education Institutions Research Program (NO. 20 220 815 153 728 002), Z.F. acknowledges the support from the New Cornerstone Science Foundation through the XPLORER PRIZE and Hong Kong Alliance of Technology and Innovation through BOCHK Science and Technology Innovation Prize.

Conflict of Interest

The authors declare no conflict of interest.

Author Contributions

Y.L. and Z.F. conceived the idea of the work. S.M. performed the device fabrication, optimization, electrical measurement, and data analysis with assistance from C.W. and Z.S. Z.W. developed the circuit and user interface. S.M. and D.Z. delivered the SEM and EDS characterization. Y.D. performed the schematic drawing. S.M. performed subject studies with the help from L.S. C.L., J.C., L.H., and Z.Y. contributed to the investigation of circuit design. S.M., C.W., Z.S., Y.L., and Z.F. wrote the manuscript. All authors provided feedback on the results and the paper.

Data Availability Statement

The data that support the findings of this study are available from the corresponding author upon reasonable request.

Keywords

in-array bio-signals calibration, inkjet printing, interpenetrating interfaces, sweat analysis, wearable biosensors

Received: October 23, 2023
Revised: February 8, 2024
Published online:

---

[1] J. Kim, A. S. Campbell, B. E.-F. de Ávila, J. Wang, *Nat. Biotechnol.* **2019**, *37*, 389.

[2] Y. Luo, M. R. Abidian, J.-H. Ahn, D. Akinwande, A. M. Andrews, M. Antonietti, Z. Bao, M. Berggren, C. A. Berkey, C. J. Bettinger, *ACS Nano.* **2023**, *17*, 5211.

[3] J. A. Rogers, T. Someya, Y. G. Huang, *Science.* **2010**, *327*, 1603.

[4] Y. R. Yang, W. Gao, *Chem. Soc. Rev.* **2019**, *48*, 1465.

[5] Y. Yu, H. Y. Y. Nyein, W. Gao, A. Javey, *Adv. Mater.* **2020**, *3*, 1902083.

[6] L. B. Baker, *Temperature.* **2019**, *6*, 211.

[7] J. R. Sempionatto, V. R.-V. Montiel, E. Vargas, H. Teymourian, J. Wang, *ACS Sens.* **2021**, *6*, 1745.

[8] S. F. Spampinato, G. I. Caruso, R. De Pasquale, M. A. Sortino, S. Merlo, *Pharmaceuticals.* **2020**, *13*, 60.

[9] F. Tehrani, H. Teymourian, B. Wuerstle, J. Kavner, R. Patel, A. Furmidge, R. Aghavali, H. Hosseini-Toudeshki, C. Brown, F. Y. Zhang, K. Mahato, Z. X. Li, A. Barfidokht, L. Yin, P. Warren, N. Huang, Z. Patel, P. P. Mercier, J. Wang, *Nat. Biomed. Eng.* **2022**, *6*, 1214.

[10] Z. Sonner, E. Wilder, J. Heikenfeld, G. Kasting, F. Beyette, D. Swaile, F. Sherman, J. Joyce, J. Hagen, N. Kelley-Loughnane, R. Naik, *Biomicrofluidics.* **2015**, *9*, 031301.

[11] W. Gao, S. Emaminejad, H. Y. Y. Nyein, S. Challa, K. V. Chen, A. Peck, H. M. Fahad, H. Ota, H. Shiraki, D. Kiriya, D. H. Lien, G. A. Brooks, R. W. Davis, A. Javey, *Nature.* **2016**, *529*, 509.

[12] L.-C. Tai, T. S. Liaw, Y. Lin, H. Y. Nyein, M. Bariya, W. Ji, M. Hettick, C. Zhao, J. Zhao, L. Hou, *Nano Lett.* **2019**, *19*, 6346.

[13] W. Gao, H. Y. Y. Nyein, Z. Shahpar, H. M. Fahad, K. Chen, S. Emaminejad, Y. J. Gao, L. C. Tai, H. Ota, E. Wu, J. Bullock, Y. P. Zeng, D. H. Lien, A. Javey, *ACS Sens.* **2016**, *1*, 866.

[14] H. Y. Y. Nyein, M. Bariya, B. Tran, C. H. Ahn, B. J. Brown, W. B. Ji, N. Davis, A. Javey, *Nat. Commun.* **2021**, *12*, 1823.

[15] D. Keilin, E. Hartree, *Biochem. J.* **1952**, *50*, 331.

[16] P. Goswami, S. S. R. Chinnadayyala, M. Chakraborty, A. K. Kumar, A. Kakoti, *Appl. Microbiol. Biotechnol.* **2013**, *97*, 4259.

[17] M. R. Ely, R. W. Kenefick, S. N. Cheuvront, T. D. Chinevere, C. P. Lacher, H. C. Lukaski, S. J. Montain, *J. Appl. Physiol.* **2011**, *110*, 1534.

[18] P.-H. Lin, S.-C. Sheu, C.-W. Chen, S.-C. Huang, B.-R. Li, *Talanta.* **2022**, *241*, 123187.

[19] M. J. Buono, *Exp. Physiol.* **1999**, *84*, 401.

[20] A. J. Bandodkar, D. Molinnus, O. Mirza, T. Guinovart, J. R. Windmiller, G. Valdes-Ramirez, F. J. Andrade, M. J. Schoning, J. Wang, *Biosens. Bioelectron.* **2014**, *54*, 603.

[21] P. J. Derbyshire, H. Barr, F. Davis, S. P. J. Higson, *J. Physiol. Sci.* **2012**, *62*, 429.

[22] W. Gao, C. Yu, *Adv. Healthcare Mater.* **2021**, *10*, 2101548.

[23] S. Emaminejad, W. Gao, E. Wu, Z. A. Davies, H. Yin Yin Nyein, S. Challa, S. P. Ryan, H. M. Fahad, K. Chen, Z. Shahpar, *Proc. Natl. Acad. Sci. U. S. A.* **2017**, *114*, 4625.

[24] N. V. Emanuele, T. F. Swade, M. A. Emanuele, *Alcohol Health Res. World.* **1998**, *22*, 211.

[25] S. Kiechl, J. Willeit, W. Poewe, G. Egger, F. Oberhollenzer, M. Muggeo, E. Bonora, *BMJ.* **1996**, *313*, 1040.

[26] A. Wiorek, M. Parrilla, M. Cuartero, G. n. A. Crespo, *Anal. Chem.* **2020**, *92*, 10153.

[27] Y. Song, R. Y. Tay, J. Li, C. Xu, J. Min, E. Shirzaei Sani, G. Kim, W. Heng, I. Kim, W. Gao, *Sci. Adv.* **2023**, *9*, eadi6492.

[28] A. Bhide, S. Muthukumar, A. Saini, S. Prasad, *Sci. Rep.* **2018**, *8*, 6507.

[29] T. R. Chang, H. Li, N. R. Zhang, X. R. Jiang, X. G. Yu, Q. D. Yang, Z. Y. Jin, H. Meng, L. Q. Chang, *Microsyst. Nanoeng.* **2022**, *8*, 25.

[30] J. Kim, I. Jeerapan, S. Imani, T. N. Cho, A. Bandodkar, S. Cinti, P. P. Mercier, J. Wang, *ACS Sens.* **2016**, *1*, 1011.

[31] A. J. Bandodkar, W. Z. Jia, C. Yardimci, X. Wang, J. Ramirez, J. Wang, *Anal. Chem.* **2015**, *87*, 394.

[32] J. R. Sempionatto, M. Y. Lin, L. Yin, E. de la Paz, K. Pei, T. Sonsa-Ard, A. N. D. Silva, A. A. Khorshed, F. Y. Zhang, N. Tostado, S. Xu, J. S. Wang, *Nat. Biomed. Eng.* **2021**, *5*, 737.

[33] Y. Sui, C. A. Zorman, *J Electrochem. Soc.* **2020**, *167*, 037571.

[34] L. Gonzalez-Macia, A. Morrin, M. R. Smyth, A. J. Killard, *Analyst.* **2010**, *135*, 845.

[35] K. Yan, J. A. Li, L. J. Pan, Y. Shi, *APL Mater.* **2020**, *8*, 12.

[36] H. Hussin, N. Soin, S. F. W. M. Hatta, F. A. M. Rezali, Y. A. Wahab, *J. Electrochem. Soc.* **2021**, *168*, 077508.

[37] P. Sundriyal, S. Bhattacharya, in *Environmental, Chemical, and Medical Sensors*, Springer, New York **2018**.

[38] S. Ali, S. Khan, A. Bermak, *IEEE Access.* **2019**, *7*, 163981.

[39] D. D. Le, T. N. N. Nguyen, D. C. T. Doan, T. M. D. Dang, M. C. Dang, *Adv. Nat. Sci.: Nanosci. Nanotechnol.* **2016**, *7*, 025002.

[40] J. Perelaer, B. J. De Gans, U. S. Schubert, *Adv. Mater.* **2006**, *18*, 2101.

[41] A. Romeo, A. Moya, T. S. Leung, G. Gabriel, R. Villa, S. Sanchez, *Appl. Mater. Today.* **2018**, *10*, 133.

[42] E. Bilbao, S. Kapadia, V. Riechert, J. Amalvy, F. N. Molinari, M. M. Escobar, R. R. Baumann, L. N. Monsalve, *Sens. Actuators, B.* **2021**, *346*, 130558.

[43] A. Moya, G. Gabriel, R. Villa, F. J. del Campo, *Curr. Opin. Electrochem.* **2017**, *3*, 29.

[44] N. Komuro, S. Takaki, K. Suzuki, D. Citterio, *Anal. Bioanal. Chem.* **2013**, *405*, 5785.

[45] Z. Bedlovicova, I. Strapac, M. Balaz, A. Salayova, *Molecules.* **2020**, *25*, 3191.

[46] V. Amendola, M. Meneghetti, M. Stener, Y. Guo, S. Chen, P. Crespo, M. A. García, A. Hernando, P. Pengo, L. Pasquato, in *Comprehensive Analytical Chemistry*, Vol. *66*, Elsevier, New York **2014**, pp. 81–152.

[47] S. B. Yaqoob, R. Adnan, R. M. Rameez Khan, M. Rashid, *Front. Chem.* **2020**, *8*, 376.

[48] S. Olliges, S. Frank, P. A. Gruber, V. Auzelyte, H. Solak, R. Spolenak, *Mater. Sci. Eng., A.* **2011**, *528*, 6203.

[49] M. M. Rahman, A. J. S. Ahammad, J. H. Jin, S. J. Ahn, J. J. Lee, *Sensors.* **2010**, *10*, 4855.

[50] Y. Lin, M. Bariya, H. Y. Y. Nyein, L. Kivimäki, S. Uusitalo, E. Jansson, W. Ji, Z. Yuan, T. Happonen, C. Liedert, *Adv. Funct. Mater.* **2019**, *29*, 1902521.

[51] R. Zhao, M. Xu, J. Wang, G. Chen, *Electrochim. Acta.* **2010**, *55*, 5647.

[52] K. Hamdani, K. L. Cheng, *Microchem. J.* **1999**, *61*, 198.

[53] R. Rahimi, M. Ochoa, A. Tamayol, S. Khalili, A. Khademhosseini, B. Ziaie, *ACS Appl. Mater. Interfaces.* **2017**, *9*, 9015.

[54] M. Kaempgen, S. Roth, *J. Electroanal. Chem.* **2006**, *586*, 72.

[55] Q. F. Li, W. Tang, Y. Z. Su, Y. K. Huang, S. Peng, B. G. Zhuo, S. Qiu, L. Ding, Y. Z. Li, X. J. Guo, *IEEE Electron Device Lett.* **2017**, *38*, 1469.

[56] J. C. Charlier, P. C. Eklund, J. Zhu, A. C. Ferrari, *Top. Appl. Phys.* **2008**, *111*, 673.

[57] D. Bruen, C. Delaney, L. Florea, D. Diamond, *Sensors.* **2017**, *17*, 1866.

[58] W. T. Dang, L. Manjakkal, W. T. Navaraj, L. Lorenzelli, V. Vinciguerra, R. Dahiya, *Biosens. Bioelectron.* **2018**, *107*, 192.

[59] Y. Wang, X. Wang, W. Lu, Q. Yuan, Y. Zheng, B. Yao, *Talanta.* **2019**, *198*, 86.

[60] H. B. Yildiz, L. Toppare, *Biosens. Bioelectron.* **2006**, *21*, 2306.

[61] H. Y. Y. Nyein, W. Gao, Z. Shahpar, S. Emaminejad, S. Challa, K. Chen, H. M. Fahad, L.-C. Tai, H. Ota, R. W. Davis, *ACS Nano.* **2016**, *10*, 7216.

[62] D. K. Efetov, P. Kim, *Phys. Rev. Lett.* **2010**, *105*, 256805.

[63] E. Hwang, S. D. Sarma, *Phys. Rev. B.* **2009**, *79*, 165404.

[64] C.-H. Park, N. Bonini, T. Sohier, G. Samsonidze, B. Kozinsky, M. Calandra, F. Mauri, N. Marzari, *Nano Lett.* **2014**, *14*, 1113.

[65] J. Kim, J. R. Sempionatto, S. Imani, M. C. Hartel, A. Barfidokht, G. Tang, A. S. Campbell, P. P. Mercier, J. Wang, *Adv. Sci.* **2018**, *5*, 1800880.

[66] H. Y. Y. Nyein, M. Bariya, L. Kivimäki, S. Uusitalo, T. S. Liaw, E. Jansson, C. H. Ahn, J. A. Hangasky, J. Zhao, Y. Lin, *Sci. Adv.* **2019**, *5*, eaaw9906.

[67] Y. Khan, A. E. Ostfeld, C. M. Lochner, A. Pierre, A. C. Arias, *Adv. Mater.* **2016**, *28*, 4373.

[68] L. Wang, K. Jiang, G. Shen, *Appl. Phys. Lett.* **2021**, *15*, 119.

[69] J. Zhao, Y. Lin, J. Wu, H. Y. Y. Nyein, M. Bariya, L.-C. Tai, M. Chao, W. Ji, G. Zhang, Z. Fan, *ACS Sens.* **2019**, *4*, 1925;

[70] J. Benson, C. M. Fung, J. S. Lloyd, D. Deganello, N. A. Smith, K. S. Teng, *Nanoscale Res. Lett.* **2015**, *10*, 127.

[71] J. Chen, Y. Miao, X. Wu, *J. Colloid Sci.* **2007**, *69*, 660.

[72] X. He, L. Tian, M. Qiao, J. Zhang, W. Geng, Q. Zhang, *J. Mater. Chem. A.* **2019**, *7*, 11478.

[73] A. N. Mansour, J. K. Ko, G. H. Waller, C. A. Martin, C. Zhang, X. Qiao, Y. Wang, X. Zhou, M. Balasubramanian, *ECS J. Solid State Sci. Technol.* **2021**, *10*, 103002.

[74] H. D. Tran, Y. Wang, J. M. D'Arcy, R. B. Kaner, *ACS Nano.* **2008**, *2*, 1841.

[75] Y. Y. Liu, B. Derby, *Phys. Fluids.* **2019**, *3*, 31.

[76] MetalonTM JS-B25HV Silver Inkjet Ink Safety Data Sheet, https://www.novacentrix.com/datasheet/Metalon-JS-B25HV-SDS.pdf (accessed: June 2016).